PERGAMON

International Journal of Rock Mechanics and Mining Sciences 37 (2000) 245–262

International Journal of
Rock Mechanics
and Mining Sciences

www.elsevier.com/locate/ijrmms

Single fractures under normal stress: The relation between fracture specific stiffness and fluid flow

L.J. Pyrak-Nolte[a, b,*], J.P. Morris[a]

[a]*Department of Physics, Purdue University, 1396 Physics Building, West Lafayette, IN 47907-1396, USA*
[b]*Department of Earth and Atmospheric Sciences, Purdue University, West Lafayette, IN 47907-1397, USA*

Accepted 7 October 1999

Abstract

Fracture specific stiffness and fluid flow through a single fracture under normal stress are implicitly related through the geometry of the void space and contact area that comprise the fracture. Data from thirteen different rock samples, each containing a single fracture, show that relationships between fracture specific stiffness and fluid flow through a fracture fall into two general classes of behavior. Fractures either fall on a loosely-defined universal curve relating fluid flow to fracture specific stiffness, or else the flow is weakly dependent on fracture specific stiffness. The second relationship shows that flow decreases slowly with increasing fracture specific stiffness. The first relationship shows that flow decreases rapidly for increases in fracture specific stiffness. To understand this behavior, computer simulations on simulated single fractures were performed to calculate fluid flow, fracture displacement, and fracture specific stiffness as a function of normal stress. Simulated fractures with spatially correlated and uncorrelated aperture distributions were studied. Fractures with spatially uncorrelated aperture distributions tend to exhibit a weak dependence of fluid flow on fracture specific stiffness because these fractures tend to have multiple connected paths across the sample which can support flow with uniformly distributed contact area. Thus an increment in stress will increase the stiffness of the fracture without greatly reducing the amount of fluid flow. On the other hand, fractures with spatially correlated aperture distributions tend to belong to the universal relationship because correlated fractures tend to have only one or two dominant flow paths and the contact area is limited to a few regions resulting in a compliant fracture. Thus an increment in stress on a spatially correlated fracture will result in an increase in stiffness and rapid decrease in fluid flow. These spatial correlations in fracture void geometry can be differentiated in the laboratory based on the observed fracture specific stiffness–fluid flow relationship for a single fracture under normal loading. © 2000 Elsevier Science Ltd. All rights reserved.

1. Introduction

In his Jaeger Lecture [1], Prof. Neville G. W. Cook wrote:

> "Intuitively, the effect of joints on mechanical, hydraulic, and seismic properties is primarily a function of the geometry of the asperities of contact between two rough surfaces and of the void spaces adjacent to these asperities."

This concept is embodied in Fig. 1 [2] which shows four direct relationships between the mechanical and hydraulic properties of a single fracture subjected to normal stress. These relationships are: (1) fluid flow through the fracture depends on the aperture distribution of the fracture; (2) flow through a fracture depends on the contact area of the fracture; (3) fracture specific stiffness depends on the amount and spatial distribution of the contacts; and (4) fracture specific stiffness depends on the aperture distribution of the fracture. Because fluid flow and fracture specific stiffness depend on the geometry of the fracture through the size and spatial distribution of the aperture and the contact area, *fluid flow* through the fracture and fracture *specific stiffness* must be implicitly

* Corresponding author. Tel.: +1-765-494-3027; fax: +1-765-494-0706.
E-mail address: ljpn@physics.purdue.edu (L.J. Pyrak-Nolte).

1365-1609/00/$ - see front matter © 2000 Elsevier Science Ltd. All rights reserved.
PII: S1365-1609(99)00104-5

related. The link between fluid flow and fracture specific stiffness is important in developing seismic interpretation methods for predicting the hydraulic response of a fracture from seismic wave attenuation and velocity. Thus, in principle, the demonstration of the link between fluid flow and fracture specific stiffness will enable a direct link between the seismic response of a fracture and the hydraulic characteristics of the fracture.

In this paper, we investigate numerically the interrelationship between fracture specific stiffness and fluid flow through a single fracture. We find that the interrelationship between fracture specific stiffness and fluid flow is intimately linked to the spatial correlation of the aperture distribution in the fracture. For fractures with aperture distributions that have long-range correlations, the flow decreases rapidly with changes in fracture specific stiffness. Fractures with aperture distributions that have short-range spatial correlations result in an interrelationship where flow is less sensitive to changes in fracture specific stiffness, and decreases slowly with increases in fracture specific stiffness.

2. Direct relationships among fracture properties

To uncover the implicit relationship between fluid flow and fracture specific stiffness, it is first necessary to quantitatively establish the individual direct relationships illustrated by Fig. 1. A *direct relationship* means that one fracture property controls the other property. For example, in the first relationship, fracture aperture controls the amount of fluid flowing through a fracture. It is difficult to establish an unique function relating the hydraulic and mechanical properties of fractures because these properties both depend on the statistical distribution of aperture and contact area. Thus, we have turned to the literature for experimental measurements to find if the data support the hypothesis of a relationship between the hydraulic and mechanical properties of the fractures. The direct relationship between fluid flow and fracture aperture has been established from experimental, theoretical, and numerical investigations of fluid flow through a fracture. Lomize [3] found that laminar flow between two glass plates depends on the cube of the separation (aperture) between the plates. This relationship is the Reynolds equation for viscous flow between parallel plates and is often referred to as the cubic law. The applicability of the cubic law to flow through fractures has been explored by many investigators both experimentally and analytically [4–17]. Deviations from cubic law behavior have been attributed to irreducible flow [10], surface roughness [9,18,19], tortuosity [1,20], and a non-linear relationship between the hydraulic aperture and mechanical displacement [13]. While deviations from the cubic law have been observed, fluid flow through a fracture does depend on the aperture of the fracture. In this paper, *fluid flow* is taken as the volumetric flow per unit head drop, which is conventionally measured in the laboratory.

Much of the recent work on understanding the relationship between fluid flow and fracture aperture has focused on imaging and quantifying the aperture distributions observed in single fractures (Fig. 2). Measurements of fracture aperture have been made using a variety of techniques including x-ray tomography [21,22], surface topography [16,17,23], and void casting/injection [11,24–26]. The data in Fig. 2 show

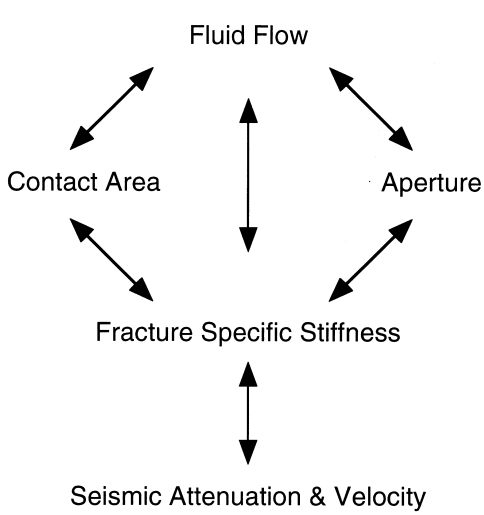

Fig. 1. Fracture specific stiffness and fluid flow through a fracture are implicity interrelated through the geometry of the fracture [2,21].

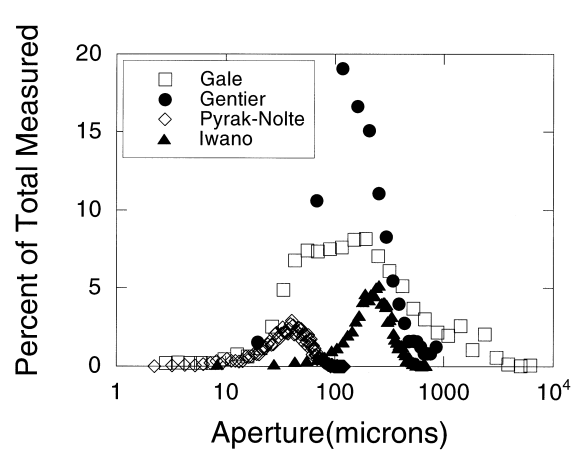

Fig. 2. Measured aperture distributions for single fractures from sample C of Keller [22], sample H1 of Gale [11], natural tensile fracture from Gentier [27], natural fracture from Iwano and Einstein [16], and data from a fracture in a coal core from Montemagno and Pyrak-Nolte [28]. The histogram is expressed in percent for comparison and the aperture is plotted on a log scale. Zero aperture is not included in the histograms.

that the aperture size distribution for single fractures can be either gaussian or log-normal. In Fig. 2 the percent of apertures of a certain size is shown for four fractures taken from the literature. Note that the data do not indicate the percent contact area, i.e., the percent of apertures that have zero magnitude. The aperture distributions measured by Gale [11] and Gentier [27] were observed to have a log-normal distribution while those measured by Iwano and Einstein [16] and Montemagno and Pyrak-Nolte [18] were observed to have a gaussian distribution. It is recognized that an accurate map of the aperture distribution and contact area in a fracture would aid in the accurate prediction of fluid flow through fractures. However, obtaining this information on the laboratory scale, let alone on the field scale, is usually invasive or destructive. Thus, some alternative fracture property related to fluid flow, and which is easier to measure, is needed.

Only a few investigations have studied the second direct relationship that relates fluid flow to contact area. In this paper, contact area is treated separately from the aperture distribution, i.e., contact area is not treated as a subset of a continuous aperture distribution. Contact area (or zero aperture) is a discontinuity (a delta function) in the aperture distribution function (Fig. 3) and provides a functionally distinct contribution to the mechanical behavior of a fracture. Fig. 3 shows the aperture distribution for a single frac-

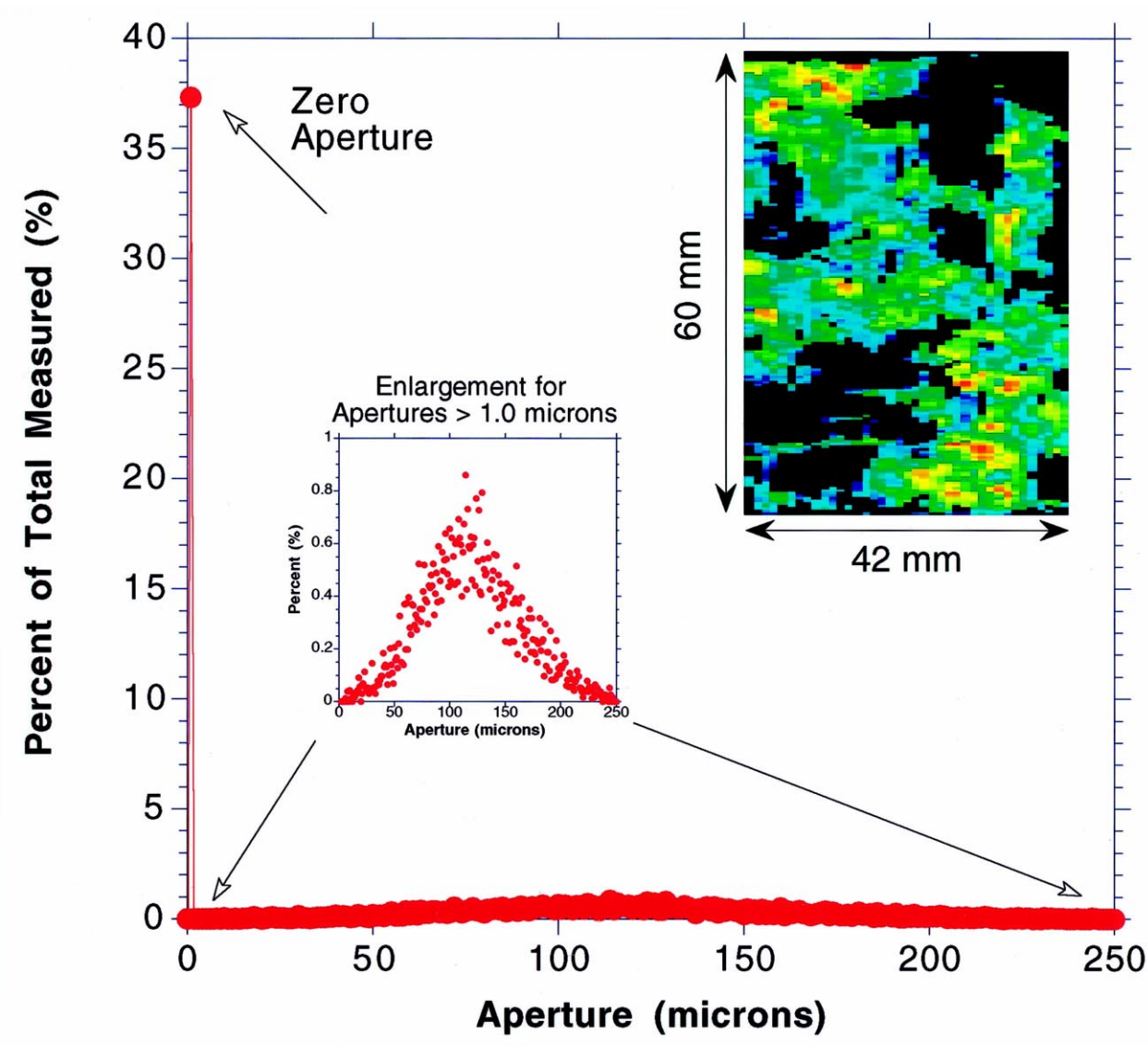

Fig. 3. Measured aperture distributions for a single fracture from a coal core sample Montemagno & Pyrak-Nolte [28] including data for regions with zero aperture. The inset is an image of the spatial distribution of apertures in the single fracture with red regions representing large apertures and blue regions representing small apertures. Black regions represent areas of rock to rock contact. The percent of apertures with zero apertures is indicated by the arrow.

ture for a coal core [28] and also shows an image of the spatial distribution of apertures within the fracture. Zero aperture regions account for almost 40% of the aperture distribution.

Methods to measure contact area as a function of normal loading have involved pressure-sensitive paper [29], deformable films [5,30] and photomicroscopy of Wood's-metal injected fractures [10]. Pyrak-Nolte et al. [10] quantitatively measured how fluid flow through the fracture decreased as contact area increased. As stress on the fracture increased, the apertures of the fracture were closed, thereby increasing the contact area between the two surfaces and decreasing the connectivity of the void space. Percolation studies on the spanning probability of void space in simulated fractures show theoretically that the probability of having a connected path across a fracture decreases with increasing contact area [31]. Zimmerman et al. [32] show from a numerical investigation that at a critical stress (around 30–70 MPa) the percolation limit is reached, i.e., a connected path across a fracture does not exist resulting in a precipitous drop in fluid flow.

The third and fourth direct relationships that relate fracture specific stiffness to contact area, and fracture specific stiffness to displacement, have been studied by several investigators through measurements of asperities or surface roughness, and theoretical and numerical analysis of asperity deformations [1,30,33–37]. Fracture specific stiffness is defined as the ratio of the increment of stress to the increment of displacement caused by the deformation of the void space in the fracture. As stress on the fracture increases, the contact area between the two fracture surfaces also increases, increasing the stiffness of the fracture. Fracture specific stiffness depends on the elastic properties of the rock and depends critically on the amount and distribution of contact area in a fracture that arises from two rough surfaces in contact [36,38,39]. Kendall and Tabor [40] showed experimentally and Hopkins et al. [38,39] have shown numerically that interfaces with the same amount of contact area but different spatial distributions of the contact area will have different stiffnesses. Greater separation between points of contacts results in a more compliant fracture or interface.

The fourth direct relationship relates fracture specific stiffness to aperture. Through measurements of fracture displacement, Bandis et al. [30] and Pyrak-Nolte et al. [10] have observed experimentally that more compliant fractures tended to have larger apertures, i.e., fractures with larger displacements for a given stress increment tend to have larger apertures. In addition to this experimental evidence for the fourth relationship, it can be demonstrated analytically (using conservation of volume [13] to determine far-field displacements for a distribution of apertures) that fractures with larger apertures will exhibit greater displacements and hence be more compliant. Zimmerman et al. [32] noted (for a penny-shaped crack) that fracture specific stiffness does not explicitly depend on fracture aperture, but does depend on the rate of formation of new contact area caused by an increase in normal stress. The rate of formation of new contact area is a direct function of the aperture distribution, and directly affects the displacement of the fracture under normal load. Thus, the aperture distribution of a fracture should directly affect the fracture specific stiffness.

Sufficient experimental and theoretical evidence exists to support the four direct relationships illustrated in Fig. 1. Because of these direct relationships, fluid flow through the fracture is implicitly related to the fracture specific stiffness through the geometry of the fracture, i.e., both of these fracture properties depend on the size and spatial distribution of the apertures, and the distribution of contact area. Pyrak-Nolte and co-workers [21,41] presented experimental evidence to support a quantitative interrelationship between fracture specific stiffness and fluid flow through a fracture, i.e., a fracture with a high specific stiffness will support less fluid flow than a more compliant fracture. In the next section, the experimental data is presented to demonstrate the implicit relationship between fluid flow and fracture specific stiffness. The experimentally determined data show that this implicit relationship is not unique, and it should not be expected to be unique because fracture geometry depends on the statistical distributions of apertures (both spatial and size) and contact area (spatial). However, it will be shown later in this paper that the slope of the fluid flow–fracture specific stiffness curve is affected by the spatial correlations in the fracture aperture distribution.

Understanding the implicit relationship between fluid flow and fracture specific stiffness is important for determining the hydraulic properties of fractures from seismic measurements. Measurements of seismic velocity and attenuation [42,43] can be used to determine remotely the specific stiffness of a fracture in a rock mass. If the implicit relationship between fluid flow and fracture specific stiffness holds, seismic measurements of fracture specific stiffness can provide a tool for predicting the hydraulic properties of a fractured rock mass. It is this implicit relationship between fracture specific stiffness and fluid flow that will be further examined in this paper using previously published data for thirteen different rock cores and a numerical investigation of deformation and fluid flow through simulated fractures.

3. Fracture specific stiffness and fluid flow through a fracture as a function of normal stress

Hydraulic and mechanical data were taken from the

Table 1
Sample name, source of data reference, sample dimensions, rock type, and type of flow measurement for each sample used in the analysis

Sample name	Reference	Sample dimensions (length, diameter)	Rock type	Flow measurement
H1	[11]	0.338 m, 0.159 m	Granite, URL, Manitoba	Radial
STR2	[11]	0.483 m, 0.152 m	Stripa Granite	Radial
S9	[44]	0.3 m, 0.15 m	Granitic Gneiss	Radial
S10	[44]	0.3 m, 0.15 m	Granitic Gneiss	Radial
S33	[44]	0.3 m, 0.15 m	Granitic Gneiss	Radial
Sample 1	[9]	0.7 m, 0.100 m	Charcoal Black Granite, Coldsprings, Minnesota	Radial
Sample 2	[9]	0.7 m, 0.150 m	Charcoal Black Granite, Coldsprings, Minnesota	Radial
Sample 3	[9]	0.7 m, 0.193 m	Charcoal Black Granite, Coldsprings, Minnesota	Radial
Sample 5	[9]	0.7 m, 0.294 m	Charcoal Black Granite, Coldsprings, Minnesota	Radial
E30	[10]	0.07 m, 0.052 m	Stripa Granite	Diametric
E32	[10]	0.07 m, 0.052 m	Stripa Granite	Diametric
E35	[10]	0.07 m, 0.052 m	Stripa Granite	Diametric
Granite	[7]	length = 0.207 m, width = 0.121 m, height = 0.155 m	Granite	Straight flow

literature to establish the existence of an interrelationship between fracture specific stiffness and fluid flow through a fracture. The data for thirteen samples have been obtained from Witherspoon et al. [7], Raven and Gale [9], Gale [44], Gale [11], and Pyrak-Nolte et al. [10]. Table 1 lists the sample name, source of the data, rock type, sample dimensions, and type of flow measurement made. All of the samples were granite and all of the studies used an applied normal load only. The values of fluid flow and fracture displacement were obtained from published data and fracture specific stiffnesses were determined numerically from the inverse of the slope of the displacement–stress curves for each sample. In previous work on the interrelationships among fracture properties, Pyrak-Nolte [40] used values of fluid flow that were corrected for irreducible [13] or residual flow. In this paper, no correction is made for irreducible flow. Data for fluid flow and fracture displacement were used from the first loading cycle. While the first loading cycle may not be the most indicative behavior of a fracture, it represents the simplest loading condition, i.e., two surfaces coming into contact. Additional unloading and loading of a fracture can result in time-dependent effects [48] with long time constants that may not have been accounted for during the experiments.

Traditionally, investigators have examined the mechanical and hydraulic properties of a single fracture as a function of stress and then developed relationships between stress and flow or stress and displacement. Fig. 4 shows the flow per unit head as a function of normal stress for all of the fracture samples listed in Table 1. All of the fractures exhibited a decrease in the amount of fluid flow with increasing normal stress on the fracture. As stress is applied, the apertures are reduced in size and the contact area increases, thereby

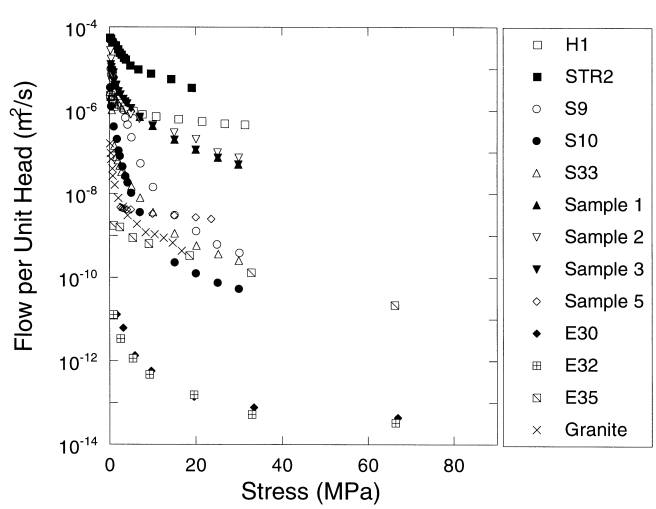

Fig. 4. Flow per unit head as a function of normal stress for thirteen different samples (see Table 1) each containing a single fracture.

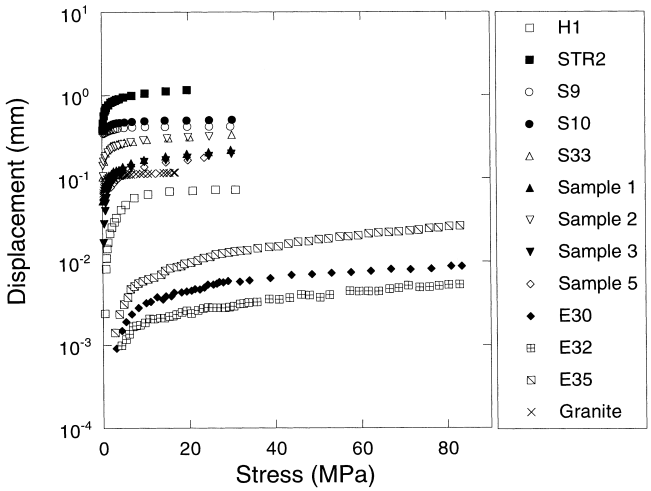

Fig. 5. Displacement as a function of applied normal stress for thirteen different samples (see Table 1) each containing a single fracture. The flow per unit head for these samples is shown in Fig. 4.

reducing the flow. While all of the samples exhibit the same qualitative trends, the amount of flow among the fracture samples varies over nine orders of magnitude. Similarly, the displacement (Fig. 5) and the fracture specific stiffness (Fig. 6) for all of the fracture samples exhibit the same qualitative trends with increasing applied normal load but vary in the amount of displacement by tens to hundreds of microns. By examining the data as a function of stress, all of the fractures appear to behave very differently and any interrelationship among the fracture properties is obscured. This arises because stress is not the link between the hydraulic and mechanical properties of a fracture. The link between these properties is the fracture geometry and how it deforms under stress. For instance, by comparing the mechanical deformation data and fracture specific stiffness (Figs. 5, 6), it is observed that the fracture with largest displacement (STR2) is the most compliant (lowest stiffness) of all of the fractures. In addition, sample STR2 supports the most fluid flow (Fig. 4). For a fracture to exhibit large displacements, it must contain large apertures and few regions of contact, and thus would support more fluid flow. Conversely, samples E30 and E32 exhibited the smallest amount of displacement, had the highest stiffness but supported the least amount of fluid flow.

4. Interrelationship between fracture specific stiffness and fluid flow

In the previous section, it was shown that the interrelationship among fracture properties was obscured by examining the data as a function of stress. The data for the thirteen fracture samples is re-examined based on the hypothesized implicit interrelationship between fracture specific stiffness and fluid flow per unit head (Fig. 1). Data from the thirteen fracture samples resulted in the fluid flow–fracture specific stiffness relationship shown in Fig. 7. The fluid flow–fracture specific stiffness interrelationship spans several orders of magnitude in the amount of flow and the value of fracture specific stiffness for samples ranging in size from 0.052 to 0.295 m. All of the data shown in Fig. 7 are from the first loading cycle (see previous section) and the fluid flow measurements are not corrected for irreducible flow. There appears to be two types of phenomenological behaviors between fracture specific stiffness and flow. The first behavior is exhibited by the data from samples STR2, S9, S10, S33, Sample 1, Sample 2, Sample 3, E30, E32, E35 which tend to fall on a sigmoidal curve that shows a nine-order-of-mag-

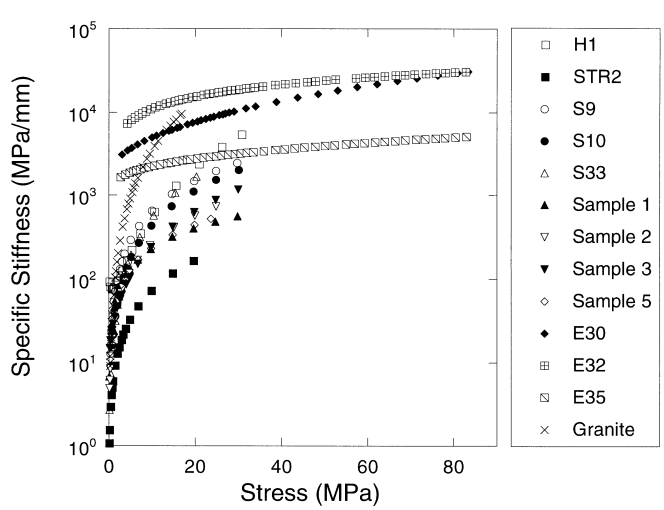

Fig. 6. Fracture specific stiffness as a function of normal stress for the same thirteen samples as shown in Figs. 4 and 5.

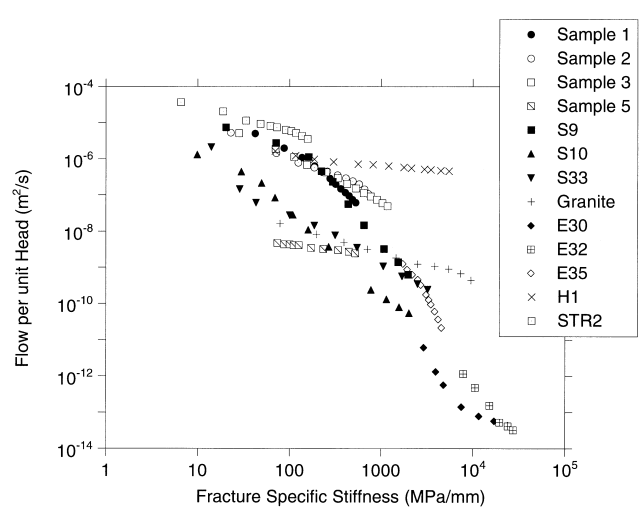

Fig. 7. Fluid flow per unit head as a function of normal fracture specific stiffness for thirteen fracture sample (see Table 1).

nitude decrease in flow with a three order of magnitude increase in fracture specific stiffness. The second behavior illustrated by fracture samples H1, Sample 5, and Granite, shows that the flow is less dependent on stiffness or stress, i.e., the magnitude of the slope of the fluid flow–fracture specific stiffness curve is less than unity.

To understand the source of the two observed fluid flow–fracture specific stiffness behaviors illustrated by the data in Fig. 7, a numerical approach is taken to determine the role of fracture void geometry on this interrelationship. Numerical models for fracture deformation and fluid flow through the fracture are applied to simulated fractures with known geometrical properties.

5. Simulation of fracture geometry

Spatially correlated and uncorrelated aperture distributions were generated using a hierarchical construction of the fracture aperture distribution known as stratified percolation [31]. The stratified percolation method for generating synthetic two-dimensional fractures is performed by a recursive algorithm that defines a self-similar cascade. Classical random continuum percolation is applied on successively smaller scales (tiers). Several (n-points per tier) randomly positioned, equal size squares are chosen within the array defining the fracture plane (the first tier). Within each square (the second tier), n smaller squares are chosen. The sub-squares are reduced in linear size by a constant scale factor relative to the previous tier square size. This recursive process is continued until the final tier is reached. This recursive construction approach leads to long-range spatial correlations in the aperture distribution because regions of non-zero aperture can only occur within squares selected on tiers throughout the hierarchy. Each time a point overlaps a previously plotted point, the aperture is increased one unit. The final aperture array is proportional to the density of sites. The range of the spatial correlation of the aperture distribution is a function of the number of tiers used to construct the pattern. For example, a one tier pattern is equivalent to a random distribution of apertures that is spatially uncorrelated, i.e., the correlation is very short on the order of one pointsize. Conversely, a five tier pattern results in an aperture distribution that has long range correlations, i.e., the correlation length extends almost across the entire pattern.

In this study of the effect of fracture void geometry on the fluid flow–fracture specific stiffness relationship, all of the simulated fractures consisted of a 300 by 300 pixel array. The number of tiers, and points per tier are given in Table 2. In the rest of this paper, the one-tier pattern will be referred to as uncorrelated and the 5-tier pattern will be referred to as correlated, with the degree of correlation related to the number of points per tier. The simulated fractures were assumed to be 0.1 m a side and had a pore volume of 1×10^{-6} m^3. A constant void volume was used for both the correlated and uncorrelated simulated fractures, i.e., the amount of void volume was constant but the distribution of the volume differed.

The first row of images in Fig. 8 shows representative realizations of the simulated fractures (based on the parameters in Table 2) at zero stress. In Fig. 8, the color represents the size of the aperture with red–yellow representing large apertures and purple–blue representing small apertures. White regions in the images of the simulated fractures represent contact area. The aperture histogram for each simulated fracture for each stress (no stress, 20 and 40 MPa) is shown in Fig. 9. The histograms represent the fraction of the total number of apertures with a given aperture size. The bin width in Fig. 9 is 10 microns and zero aperture (contact area) is included in the first bin.

The uncorrelated (1 tier) fracture consists of a random distribution of apertures and contact area. The two correlated patterns (5-tier 10 points per tier and 5-tier 15 points per tier) have one or two dominant flow paths and fewer but larger regions of contact than the uncorrelated pattern. The uncorrelated pattern has a narrow size distribution of apertures that are widely distributed spatially in order to have the same void volume as the correlated pattern. The correlated pattern has a broad size distribution of apertures with larger apertures that occur in clumps.

6. Fracture deformation model

To explore the interrelationship between fracture specific stiffness and fluid flow through a fracture, it is necessary to determine the deformation of the fracture void space when a fracture is subjected to a normal load. In this study, the deformation of the fracture aperture distribution as a function of load is simulated using a numerical model similar to that of Hopkins [45]. Using this approach, the fracture is modeled by two half-spaces separated by an arrangement of cylindrical asperities (Fig. 10). The asperities are arranged on a regular lattice with heights determined by the aperture distribution generated by the stratified percolation algorithm (Fig. 10a). The radii of the asperities were set such that they almost touch initially. For a fracture measuring 0.1 m represented by 300 by 300 asperities, this gives an asperity radius of $0.1\dot{6}$ mm. For this analysis, the physical properties of granite were assumed and are listed in Table 3.

In this analysis, as the surfaces of the fracture are brought together under small increments of normal

Table 2
Parameters used in the stratified percolation model to generate simulated fractures with spatially correlated and uncorrelated aperture distributions

Fracture type	Number of tiers	Points per tier	Point size	Scale factor
Uncorrelated	1	10^5	4	75
Correlated: 8pt	5	8	4	2.37
Correlated: 10pt	5	10	4	2.37
Correlated: 15pt	5	15	4	2.37

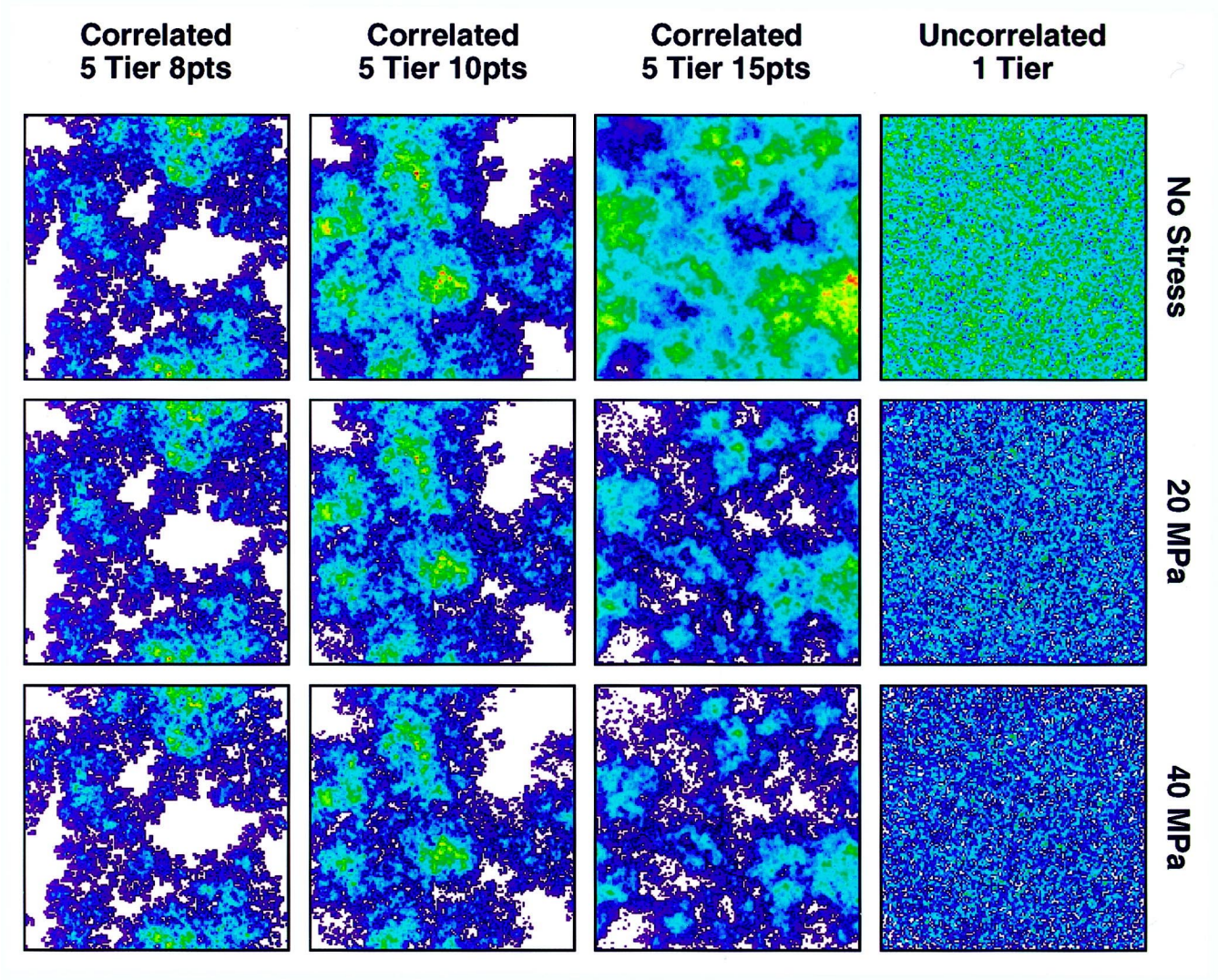

Fig. 8. Representative images of the geometry of spatially correlated and uncorrelated aperture distributions for the simulated fractures. In the images, white regions represent contact area, and increasing shades from purple to red represent increasing aperture (red represents the largest apertures, and purple the smallest apertures). The same color scale was used for all three stresses but varies among the 1 tier, 5 tier 8 points, 5 tier 10 points, and 5 tier 15 points simulated fractures. From right to left are uncorrelated fracture 1 tier, 5 tier 15 points correlated fracture, and 5 tier 10 points correlated fracture, and 5 tier 8 points correlated fracture. The images from top to bottom show the effect of increasing normal stress on the fracture (No stress, 20 and 40 MPa). As stress on a fracture is increased the apertures are reduced in size and the contact area increases. The uncorrelated fracture is composed of multiple flow paths while the correlated fractures are composed of one or two dominant flow paths. Histograms of the aperture distribution for each image are given in Fig. 9.

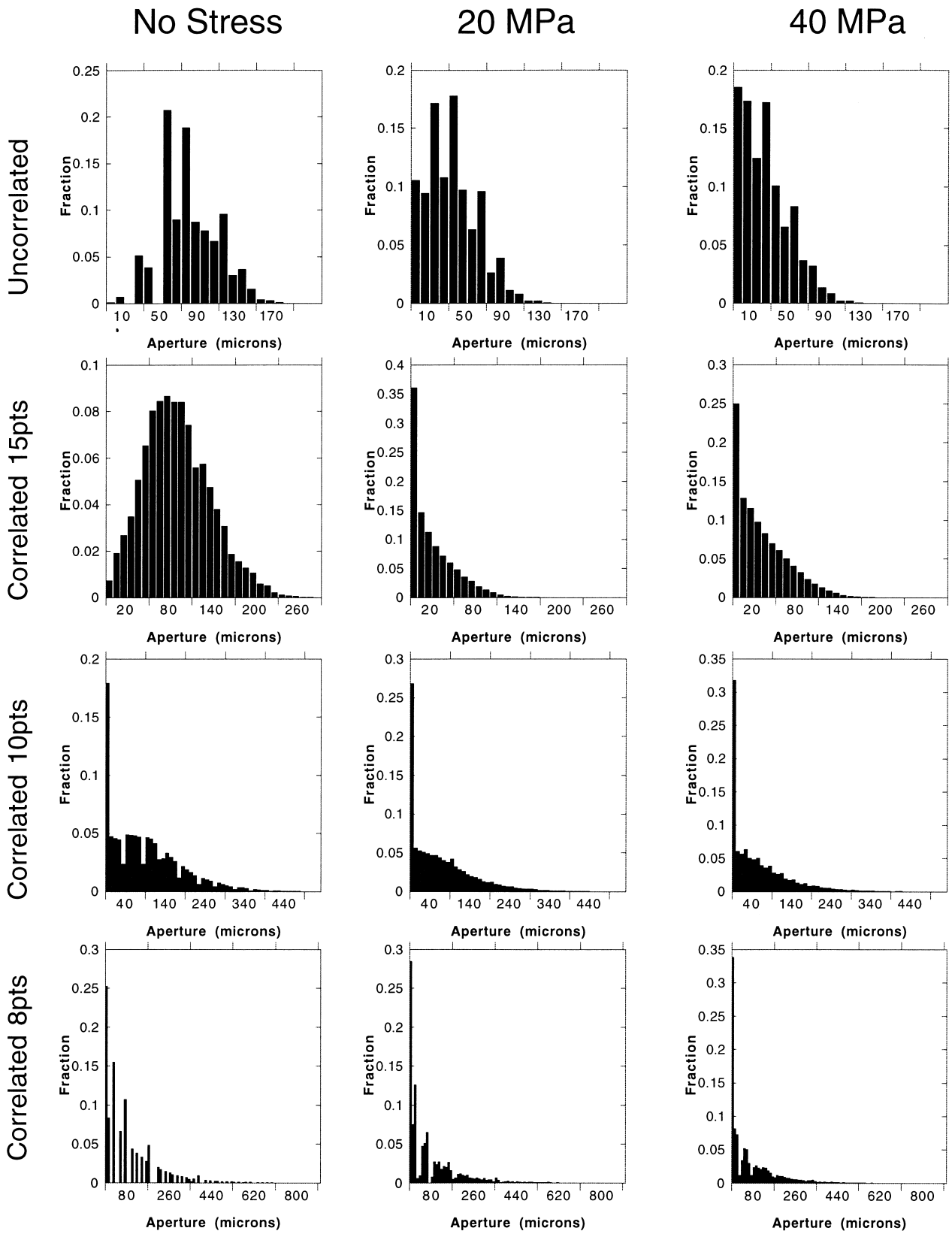

Fig. 9. The aperture distribution as a function of stress for the simulated fractures shown in Fig. 8 for no stress, and normal stresses of 20 and 40 MPa. The bin width is 10 microns. Contact area or zero aperture is included in the first bin.

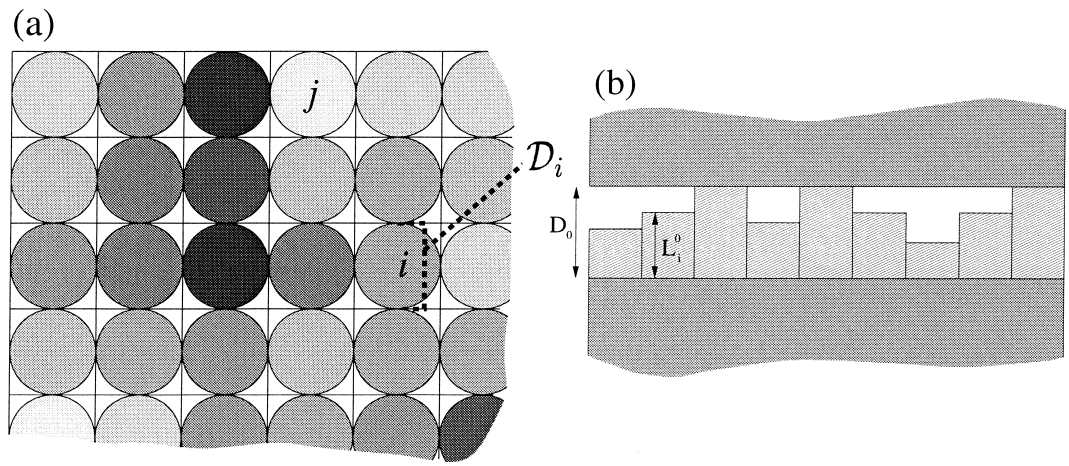

Fig. 10. (a) The fracture is approximated by circular cross-section asperities arranged on a regular grid. (b) The asperities separate two semi-infinite half-spaces initially separated by a distance D_0.

loads, the half-spaces and asperities are assumed to deform elastically as the load is varied. To model this deformation, the normal displacement [46] of a half-space at a distance r from the center of a uniformly loaded circle is used:

$$w_{\frac{1}{2}} = f\frac{4(1-\nu^2)}{\pi^2 Ea}\left(\frac{r}{a}\right)I_2\left(\frac{r}{a}\right), \tag{1}$$

where f is the force acting in the asperity, a is the radius of the circle, and

$$I_2(s) = \int_0^{\frac{\pi}{2}} \sqrt{1-\left(1/s^2\right)\sin^2\theta}\,\mathrm{d}\theta - \left[1 - \frac{1}{s^2}\right]\int_0^{\frac{\pi}{2}} \frac{\mathrm{d}\theta}{\sqrt{1-\left(1/s^2\right)\sin^2\theta}} \tag{2}$$

The term $\frac{r}{a}I_2(\frac{r}{a})$ describes the functional form of the displacement in terms of the radial distance r. Laboratory measurements of fracture deformation measure the average displacement across a fracture. In simulations of fracture displacement, it is important to determine the total displacement at each asperity that occurs from interaction of the displacement fields from neighboring asperities in order to determine the average total displacement. The average total displacement at asperity i, caused by asperity j can be written as

$$w_{ij} = f_j\frac{8(1-\nu^2)}{\pi^2 Ea}I_3(r_{ij}, a) \tag{3}$$

where f_j is the force acting in asperity j and

$$I_3(r, a) = \frac{\int_{\mathscr{D}} \frac{r'}{a}I_2\left(\frac{r'}{a}\right)r'\mathrm{d}\theta\mathrm{d}r'}{\pi a^2} \tag{4}$$

where $\mathscr{D}_i$ is the region of contact of asperity i (Fig. 10) and r' is the radial distance measured from asperity j. Here $I_3(s)$ is simply the average of $sI_2(s)$ over the region of contact of asperity i. The displacement of the half-spaces at a point is the sum of deflections due to all asperities that are in contact. In this way, each asperity in contact influences the displacement at every other asperity. The total displacement at asperity i from all of the other asperities that are in contact may be written:

$$W_i = \sum_{j\in c} w_{ij} \tag{5}$$

where c denotes the set of asperities in contact. The averaged self-contribution w_{ii} (that is the displacement caused by the deformation of asperity i) is calculated using

$$w_{ii} = f_i\frac{8(1-\nu^2)}{\pi^2 Ea}I_4(a) \tag{6}$$

where

$$I_4(a) = \frac{\int_{\mathscr{D}_i} I_1\left(\frac{r'}{a}\right)r'\mathrm{d}\theta\mathrm{d}r'}{\pi a^2} \tag{7}$$

where $\mathscr{D}_i$ is the region of contact of asperity i and

Table 3
Physical properties assumed for fracture deformation modeling

Young's Modulus	60.0 (GPa)
Poisson's ratio	0.25

$$I_1(s) = \int_0^{\frac{\pi}{2}} \sqrt{1 - s^2 \sin^2\theta}\,\mathrm{d}\theta \tag{8}$$

I_1 describes the functional form of the displacement within the region of contact of the asperity itself and is the continuation of $\frac{r}{a}I_2(\frac{r}{a})$ within $r = a$. $I_4(s)$ is simply the average of $I_1(s)$ over the region of contact of asperity i.

Once the forces acting in the asperities are determined, the change in length of the asperity is calculated from

$$\Delta L_i = f_i \frac{L_i^0}{E\pi a^2} \tag{9}$$

where $L^0{}_i$ is the unstressed length of the asperity. The force exerted by an asperity depends upon the displacement of the half-spaces which in turns depends upon the force exerted by every other asperity.

For an asperity in contact, the sum of the distance between the half-spaces in the absence of the asperities (D in Fig. 11) and the total deformation (W_i) must be equal to the length of the asperity:

$$D + W_i = L_i^0 - \Delta L_i \tag{10}$$

The W_i depends upon the forces acting in the asperities, which depends directly upon ΔL_i by Eq. (9). Thus, Eq. (10) can be written as a system of simultaneous linear equations in terms of the changes in asperity lengths. This system is large and non-sparse and difficult to solve directly. We used the Conjugate-Gradient (CG) method (see Golub and Van Loan, [47]) to solve this system (Eq. 10). The CG technique requires only an algorithm that calculates the product of the matrix with a vector, and does not require the explicit construction of a matrix representing the linear system. However, for N asperities in contact, a computational effort proportional to N^2 is needed to calculate this product. For a fracture represented using an n by n array of aperture values the solution involves order n^4 computations.

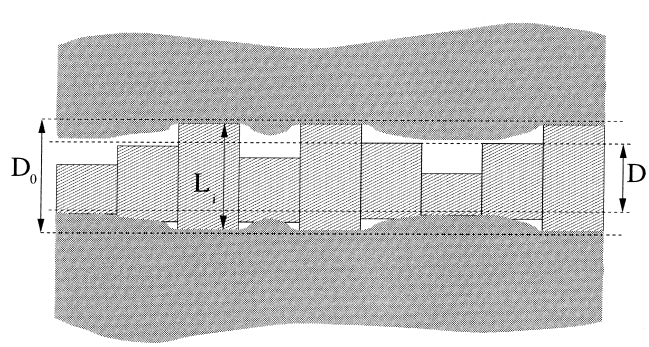

Fig. 11. The half-spaces deform elastically in response to the asperities. D is the distance which would separate the half-spaces in the absence of the asperities.

Hopkins [45] directly summed the displacements caused by the interaction of asperities but used a computationally intensive technique which limited the total number of asperities that could be used to represent a fracture. In our work, we have efficiently calculated asperity interactions using an approximate technique which allows distant contributions to be evaluated rapidly. Our approach uses a Fast Multipole Method (FMM) [49] to efficiently evaluate the matrix-vector product required by the CG method. There are other approaches which may be used to achieve high performance, for example, Unger and Mase [50] employed Fast Fourier Transforms to accelerate the calculation of the asperity interactions. However, their approach assumes rectangular asperities arranged on a regular grid while our method can be used for fractures described by irregular arrangements of asperities. For simplicity, we used a regular grid in this analysis. The Fast Multipole Method (FMM) was originally developed for particle simulations to permit long-distance interactions between N particles to be calculated in order $N \log N$ time [49]. Although more computationally expensive for small numbers of particles, this method is substantially faster than directly summing the interactions for large N.

For sufficiently large r_{ij} the average displacement due to another asperity is well approximated by the mid-point value. That is:

$$I_3(r_{ij}, a) \approx \frac{r_{ij}}{a} I_2\left(\frac{r_{ij}}{a}\right) \tag{11}$$

If we consider $I_2(s)$ for large s we find:

$$\begin{aligned} I_2(s) &= \int_0^{\frac{\pi}{2}} \left(1 - \frac{1}{s^2}\sin^2\theta\right)^{1/2} \\ &\mathrm{d}\theta - \left[1 - \frac{1}{s^2}\right] \int_0^{\frac{\pi}{2}} \left(1 - \frac{1}{s^2}\sin^2\theta\right)^{-1/2} \\ &\mathrm{d}\theta \approx \int_0^{\frac{\pi}{2}} \left(1 - \frac{1}{2s^2}\sin^2\theta\right) \\ &\mathrm{d}\theta - \left(1 - \frac{1}{s^2}\right) \int_0^{\frac{\pi}{2}} \left(1 + \frac{1}{2s^2}\sin^2\theta\right) \\ &\mathrm{d}\theta \approx \frac{1}{s^2} \int_0^{\frac{\pi}{2}} \left(1 + \sin^2\theta\right) \mathrm{d}\theta \approx \frac{\pi}{4s^2} \end{aligned} \tag{12}$$

Thus, for large r we can write

$$w_{ij} = f_j \frac{8(1-\nu^2)}{\pi^2 E a} \frac{r_{ij}}{a} \frac{\pi}{4} \frac{a^2}{r_{ij}^2} \tag{13}$$

$$= f_j \frac{2(1-\nu^2)}{\pi E} \frac{1}{r_{ij}} \tag{14}$$

We have implemented a version of FMM which calculates the interactions between asperities by evaluating multipole expansions of Eq. (14).

One complication in solving for fracture displacement using this method is that the number and location of the asperities that are in contact must be known before the system of equations is constructed. Hopkins [45] reformulated the problem as a constrained, energy minimization problem to avoid this complication. In our work, the load and aperture distribution are solved as the two surfaces are brought closer together by small increments ("steps"). This makes it possible to predict which asperities will come into contact, based upon the previous step. Because the asperity length is solved iteratively using the CG method, the results from the previous step are used as an initial guess for the solution. The asperities are then checked to see if any should be brought into contact, or removed from being in contact. The CG method is then used again to improve the current solution. This process is repeated until the solution has converged.

The specific fracture stiffness, κ, is equal to the change in stress divided by the change in displacement of the fracture. We can calculate the displacement numerically using,

$$\delta = \sum_i \delta_i / N, \tag{15}$$

where

$$\delta_i = \begin{cases} (D_0 - D) - W_i, & \text{if not in contact} \\ (D_0 - L_i^0) + \Delta L_i, & \text{if in contact} \end{cases} \tag{16}$$

where D_0 is the zero-stress spacing of the half-spaces. The stiffness can then be written

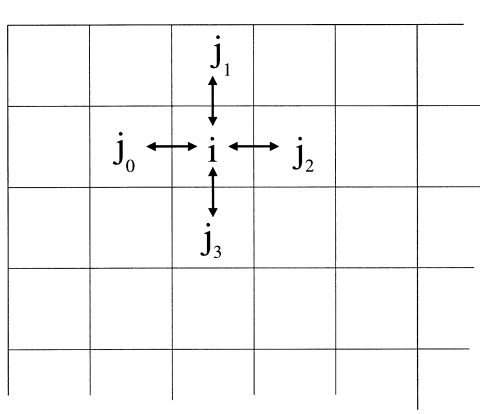

Fig. 12. The "lattice-grid" algorithm generates a network of pipes. Pixel i is joined to neighboring pixels by pipes with conductances given by flow between parallel plates.

$$\kappa = \frac{\Delta\sigma}{\Delta\delta} \tag{17}$$

using the changes in σ and δ from one step to the next.

7. Fracture fluid-flow model

The flow properties of the fractures were predicted numerically using a network model similar to that of Yang et al. [51] and Tran [52]. This method replaces the fracture with a network of pipes to approximate the flow properties of the fracture. A "lattice-grid" method was used to create pipes linking each pixel (which represents a single aperture) of the fracture with neighboring apertures (see Fig. 12). The conductance of the pipes is calculated based upon the analytic solution for flow between two parallel plates. The flow from pixel i to pixel j is:

$$q_{ij} = \frac{W b_{ij}^3}{12\mu} \frac{p_i - p_j}{L} = c_{ij}(p_i - p_j) \tag{18}$$

where W is the width of the plates (in the direction perpendicular to flow and perpendicular to the aperture), L is the length in the direction of flow, b_{ij} is the separation of the fracture surfaces (i.e., the aperture), μ is the viscosity of the fluid, p_i is the pressure at the center of pixel i, and c_{ij} is the conductance from pixel i to pixel j. The separation of the plates is taken to be the average of the aperture in the adjacent pixels:

$$b_{ij} = \frac{1}{2}(\mathrm{ap}_i + \mathrm{ap}_j) \tag{19}$$

where ap_j is the aperture at pixel i. We require that the net flow out of each pixel (i) be zero:

$$\sum_j q_{ij} = \sum_j c_{ij}(p_i - p_j) = 0 \tag{20}$$

Generating an equation of the form of Eq. (20) for each pixel gives a sparse system of linear equations to be solved for the pressure at each pixel. Once the pressure is known, the fluxes can be readily calculated. For an N by N array, this method leads to $O(N^2)$ linear equations. It is possible to reduce the computational effort by generating a network of elliptical cross-section pipes which approximate the shape of the fracture [51–53]. For this work, the flow calculation was considerably more rapid than the calculation of the mechanical deformation of the joint, and the lattice grid approach was considered sufficiently fast.

8. Spatial correlation analysis approach

Fluid flow through a fracture and fracture deformation both depend on the spatial distribution of the apertures and regions of contacts between the two fracture surfaces [12,45]. In this study, an autocorrelation analysis (based on Blair et al. [54]) was performed to quantify the correlation lengths of the different simulated fractures. The two-point autocorrelation function [54] is defined as

$$S_2(x, y) = \frac{1}{A}\int_A f(u, v) f(u + x, v + y)\, \mathrm{d}u\mathrm{d}v \tag{21}$$

where A is the total area of the fracture, and f is a function of the aperture of the fracture,

$$f_{\mathrm{ap}}(x_i, y_i) = \mathrm{ap}_i \tag{22}$$

where x_i, y_i are the co-ordinates of asperity i and ap_i is the aperture at asperity i. The function f can be defined to distinguish between contact and non-contact

$$f_0(x_i, y_i) = \begin{cases} 1, & \text{if } \mathrm{ap}_i > 0, \\ 0, & \text{otherwise} \end{cases} \tag{23}$$

The angular average [54] of $S_2(x, y)$ is defined by

$$S_2(r) = \frac{1}{2\pi}\int_0^{2\pi} S_2(r\cos\theta, r\sin\theta)\, \mathrm{d}\theta \tag{24}$$

The radial gradient of the angular average is given by

$$\frac{\mathrm{d}S_2(r)}{\mathrm{d}r} = \frac{1}{A2\pi}\int_0^{2\pi}\int_A f(u, v)\frac{f(u + r\cos\theta, v + r\sin\theta)}{\mathrm{d}r}\mathrm{d}u\mathrm{d}v\mathrm{d}\theta \tag{25}$$

Berryman [55] demonstrates that if f_0 is used, the gradient of the two-point correlation function can be used to calculate the specific perimeter s of the grain or pore of interest.

$$s = -4\frac{\mathrm{d}S_2}{\mathrm{d}r}\bigg|_{r=0} \tag{26}$$

where (in this application) the specific perimeter is defined as the ratio of the perimeter of the area of contact to the total fracture area. In our work we consider the average of S_2 calculated for many fracture realizations and approximate:

$$S_2(r) \approx S_2(r, 0) \approx S_2(0, r) \tag{27}$$

that is, we assume the autocorrelation function is isotropic. Blair et al. [54] also define a "critical lag", R_c, where the two-point correlation function intersects with ϕ^2 where is the ϕ porosity. This quantity is an indicator of the typical length over which a given pattern is correlated. In this application ϕ is taken to be the area of non-zero aperture ("area fraction"). The autocorrelation function may be calculated efficiently using Fast Fourier Transforms (FFTs) by invoking the Wiener–Khinchin theorem

$$S_2(x, y) = \mathscr{F}^{-1}|\mathscr{F}f|^2, \tag{28}$$

where $\mathscr{F}$ and $\mathscr{F}^{-1}$ denote the Fourier transform and inverse Fourier transform, respectively.

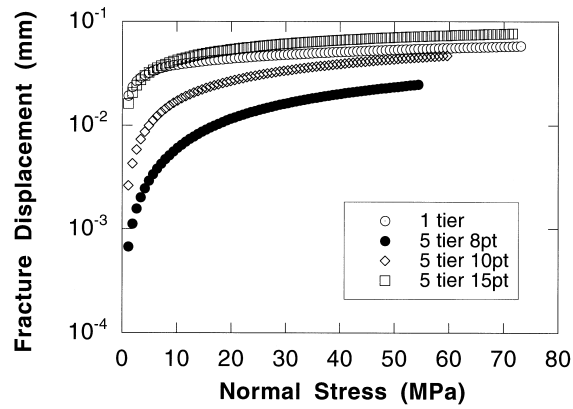

Fig. 13. Fracture displacement–normal stress curves computed for the spatially correlated and uncorrelated simulated fractures.

9. Fracture specific stiffness and fluid flow interrelationship from the numerical simulations

Figs. 13 and 14 show the average fracture displacement and the flow per unit head drop, respectively, as a function of normal load on the simulated fractures for the uncorrelated fracture (1-tier) and three correlated fractures (5-tiers with 8, 10, and 15 points per tier). Each curve in the Figs. 13 and 14 represents the average results from 10 simulations. The fracture dis-

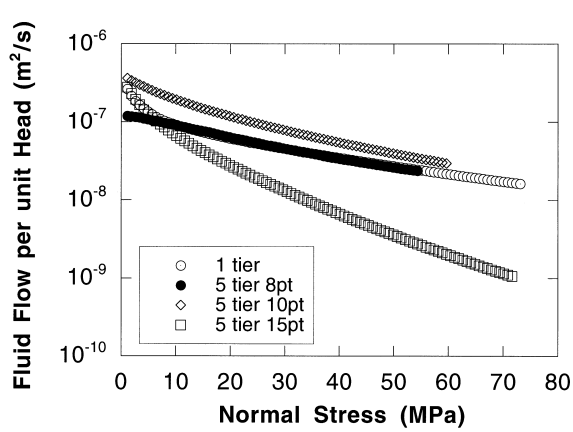

Fig. 14. Flow per unit head drop–normal stress curves computed for the spatially correlated and uncorrelated simulated fractures.

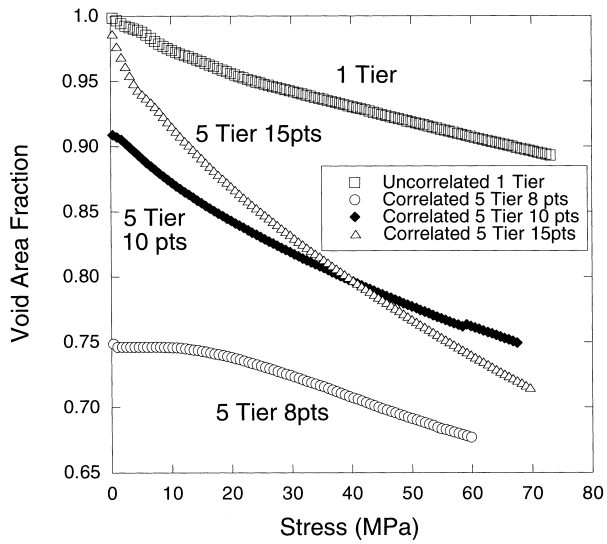

Fig. 15. Void fraction as a function of stress for the simulated fractures.

placement as a function of normal stress is observed to vary by an order of magnitude between the different simulated fractures. Though the void volumes of the fractures are the same, the size of the apertures that compose the different fractures varies because the void volume is distributed differently based on the fracture construction. The uncorrelated fracture and the 15 point per tier correlated fracture have comparable displacements and the least amount of contact area (Figs. 8 and 15). However, the amount of fluid flow through the uncorrelated and the 15 point per tier correlated fracture varies by one to one-and-one-half orders of magnitude with increasing normal stress, and the rate of decrease in flow with increasing normal stress differs between the simulated fractures.

The displacement–stress results from Fig. 13 were used to calculate the fracture specific stiffness (Fig. 16) to examine the effect of fracture void geometry on the fluid flow–fracture specific stiffness behavior. Fig. 17 shows the resulting fluid flow–fracture specific relationship for uncorrelated and correlated simulated fractures. All simulated fractures had the same void volume. Each curve represents the average of 10 simulations to reduce statistical fluctuations. The amount of fluid flow through the uncorrelated pattern (1 tier in Fig. 17) is relatively less sensitive to changes in fracture specific stiffness than the correlated patterns. The correlated simulated fractures support fluid flow that is more sensitive to changes in fracture stiffness, i.e., the correlated fracture have steeper slopes for the fluid flow–fracture specific stiffness curve than the uncorrelated (1 tier) fracture. The three correlated simulated fractures have similar slopes, and the 8 and 10 points-per-tier fractures exhibit similar behavior at high stresses. The flow rate for the 8 points-per-tier correlated fracture decreases rapidly at low stresses. The 8 point per tier simulated fracture exhibits the highest stiffness at low stresses (Fig. 16) and initially has the most contact area (Fig. 8).

Fig. 18 compares the fluid flow–fracture specific stiffness behavior from the numerical simulations to that of the data shown in Fig. 7. The uncorrelated simulated fracture supports fluid flow that is relatively less sensitive to fracture specific stiffness, i.e., though the stiffness increases significantly (about two orders of magnitude) the amount of fluid flow through the fracture decreases only about one order of magnitude. In an uncorrelated fracture, the points of contact between the two fracture surfaces are small in size and widely distributed. This distribution of contact areas results in multiple flow paths through the uncorrelated aperture distribution. As normal stress on the fracture increases, and the regions of contact grow and increase the stiffness of the fracture,

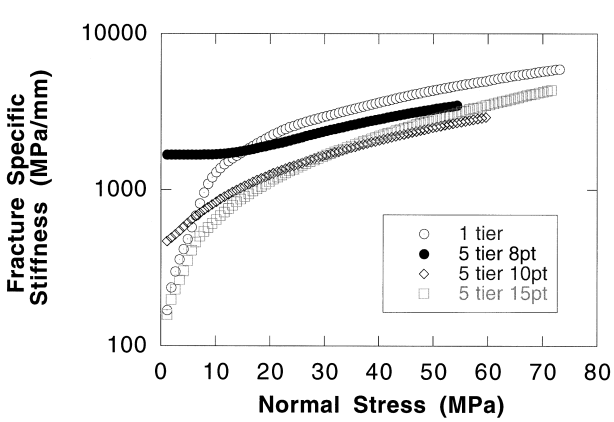

Fig. 16. Fracture specific stiffness as a function of normal stress computed for the uncorrelated (1 tier) and the correlated (5 tier 8, 10 and 15 points) simulated features.

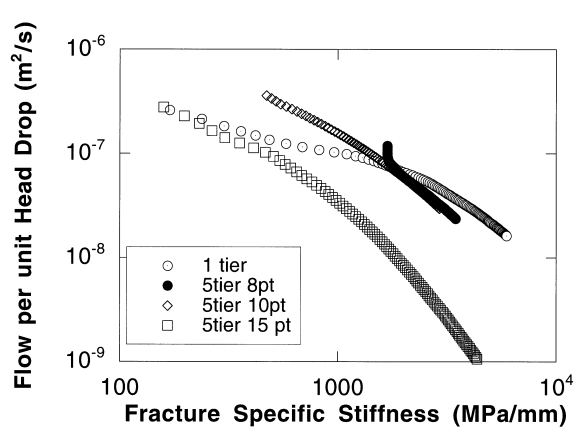

Fig. 17. Simulated fluid flow per unit head drop as a function of fracture specific stiffness for the uncorrelated simulated fracture (1 tier) and three correlated simulated fractures (5 tier with 8, 10, and 15 points per tier). Each curve is the average of 10 simulations to remove statistical fluctuations.

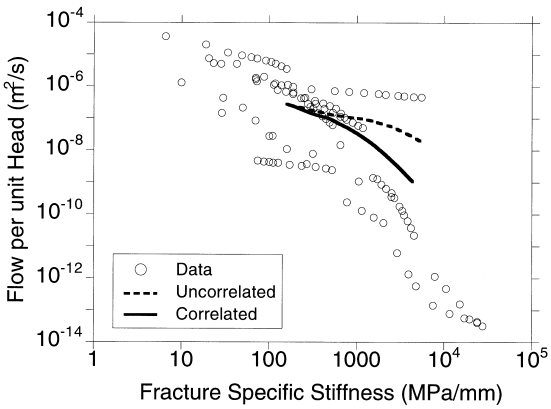

Fig. 18. Comparison of the fluid flow–fracture specific stiffness behavior determined from experimental data Fig. 7 and from the numerical simulations. The uncorrelated simulated fracture is based on a 1 tier fracture generation, and the correlated simulated fracture is based on a 5 tier 15 points per tier fracture generation.

the corresponding reduction in aperture is small. Thus, even though the apertures are reduced in size, the multiple flow paths still enable a significant amount of fluid flow to occur through the fracture.

The correlated (5 tier 15 points) fracture (Fig. 18) supports fluid flow that is relatively sensitive to changes in fracture specific stiffness. The correlated simulated fracture is composed of one or two dominant flow paths or channels (Fig. 8). Because the contact area is limited to a few regions compared with the widely distributed contact area in the uncorrelated simulated fracture, the correlated fracture at a given stress is more compliant than the uncorrelated fracture (Fig. 16). Because the flow through the fracture is restricted to one or two channels, fluid flow through the fracture will be highly sensitive to reduction in fracture apertures since there are few additional flow paths to carry fluid as in the uncorrelated fracture case.

10. Discussion

Our work suggests that the two types of fluid flow–fracture specific stiffness behavior observed in the experimental data for the thirteen samples (Fig. 7) is related to the spatial correlation of the aperture distribution. We applied an autocorrelation analysis to determine how the correlation length of the aperture distribution changed with increasing stress. In Fig. 19, the correlation length is based on the critical lag (see Autocorrelation Analysis section). The correlation length of the uncorrelated simulated fracture (1 tier) is less than 0.0025 m and remains essentially constant with increasing stress because the initial asperity distribution is uniformly distributed and remains uniformly distributed as the stress on the fracture is increased

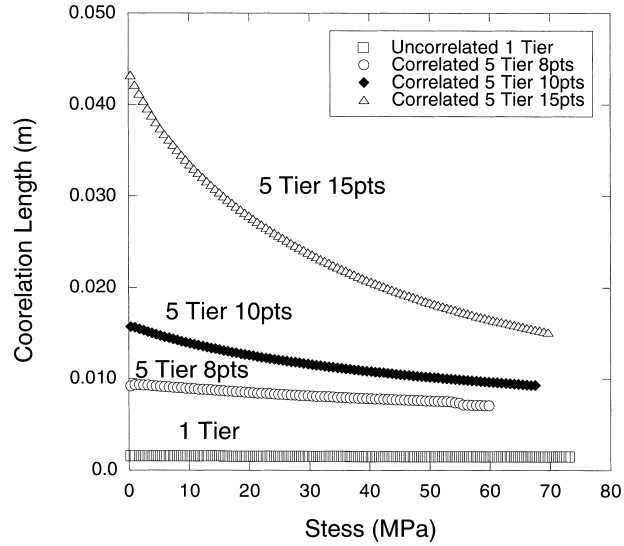

Fig. 19. A comparison of the spatial correlation length (critical lag) as a function of normal stress for the uncorrelated (1 tier) and the correlated (5 tiers 8, 10 and 15 points) simulated fractures.

(Figs. 8 and 19). The points of contact grow in size but remain relatively fixed in space and thus maintain the same multiple flow paths through the fracture.

The correlated simulated fracture (5 tiers 15 points) has a correlation length that decreases with increasing normal stress from roughly 0.04 to 0.02 m. This frac-

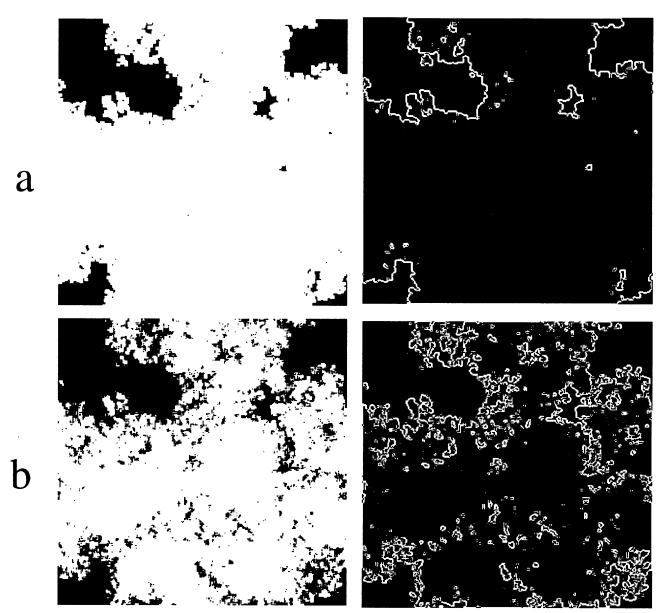

Fig. 20. The top row shows a 5 tier 10 point per tier simulated fracture at zero stress with black representing contact and white non-contact. The second row shows the same fracture under a 50 MPa load. The right columns shows these images after they have been post-processed with an edge detection routine. As the load is increased, the area in contact increases, and the perimeter separating contact from non-contact becomes more complicated in shape, leading to an increase in specific perimeter.

ture begins with a few regions of contacts localized within the fracture plane. This is observed in Fig. 20 which shows a binary image of a correlated simulated fracture for zero stress and at a stress of 50 MPa. As the normal stress on the fracture is increased, the contact area becomes more widely distributed and less confined to the original regions contact, as illustrated in Fig. 20 which is a map of the perimeters of the contact area for zero stress and for a normal stress of 50 MPa. The spatial correlation length decreases as new regions of contact are formed in the correlated fracture. This results in a pinching off of the dominant flow path in addition to the reduction in aperture that occurs as stress is applied.

Thus, it is clear that a single fracture will exhibit an individual relationship between flow and stiffness, i.e., will have its own trajectory through stiffness-flow space, but the trajectory that the fracture exhibits depends on the spatial correlations of the fracture aperture (or contact area or asperity) distribution.

Pyrak-Nolte et al. [21] found that the aperture distribution of natural fracture networks in whole-drill coal cores were spatially correlated over 10–30 mm, i.e., distances that were comparable to the size of the core samples. However, asperities on natural joint surfaces have been observed to be correlated over about 0.5 mm [56]. These two quoted values for correlations lengths vary by about two orders of magnitude. The spatial correlation length may be a function of rock type but this needs to be verified experimentally. The observation that correlations are smaller or on the same order as the sample length may explain why core samples often predict much different hydraulic–mechanical behavior than is observed in the field. If fractures on the core scale are only correlated over a few centimeters or less, the same fracture on the field scale may behave as an uncorrelated fracture. This hypothesis is suggested by the data of Raven and Gale [9] shown in Fig. 7 as Sample 1, Sample 2, Sample 3, and Sample 5. These four samples were taken from the same natural fracture in the field but differ in sample size (see Table 1). Fluid flow through Samples 1, 2, and 3 were sensitive to changes in fracture specific stiffness. However, the fluid flow through the largest sample, Sample 5, appears to be relatively insensitive to fracture specific stiffness. This suggests that the size of Sample 5 exceeded the spatial correlation length of the aperture distribution.

11. Summary and conclusions

Neville knew intuitively that the hydraulic, mechanical, and seismic properties of single fractures were interrelated through the geometry of the fracture, i.e., the shape, size, and distribution of void space. Ever since my graduate studies with Neville, I have been working on different aspects of the interrelationship among fracture properties. However, it was the initial research that formed portions of my thesis [57] that first lead us [58] to propose the interrelationship among fracture properties. From the numerical investigation presented here, the fluid flow–fracture specific stiffness behavior for a single fracture subjected to normal stress is found to depend on the spatial correlation of the aperture distribution. Thus, from measurements of this interrelationship on the laboratory scale, one may determine if the aperture distribution of the fracture is correlated or uncorrelated. Once the spatial correlations of a fracture are known, scaling theorems from percolation theory and renormalization finite-size scaling may be used to predict the fluid flow behavior as a function of scale [31,59,60].

While it is clear from the experimental data and the numerical simulations that a single fracture will exhibit a relationship between flow and stiffness, there are several broader questions. Will fractures in rocks from the same tectonic setting have the same spatial correlations in the aperture distribution? Will there be different universality classes based on rock type or stress history? Will repeated stress cycling alter the relationship? Will the relationship be scalable to the field scale? Will these results be applicable to networks of fractures? Will the different spatial correlations be detectable or measurable on the field scale using seismic or other geophysical methods. These questions cannot be addressed without more experimental results from the field and additional numerical modeling to further explore the effect of fracture geometry on fluid flow and fracture deformation, and the link to the seismic response of a fracture.

Acknowledgements

LJPN wishes to acknowledge Neville G.W. Cook for all of the insightful discussions through the years and for being a tremendous mentor! The authors also wish to acknowledge support of this research by a Young Investigator Award (EAR-9896057) from the Earth Sciences Division of the National Science Foundation and from the Geosciences Research Program, Office of Basic Energy Sciences, US Department of Energy, and from the Gas Research Institute (5095-260-4120).

References

[1] Cook NGW. Natural joints in rock: Mechanical, hydraulic, and seismic properties under normal stress. Int J of Rock Mech Min Sci & Geomech Abstr 1992;29:198–223.

[2] Pyrak-Nolte LJ. The seismic response of fractures and the interrelationships among fracture properties. International Journal of Rock Mechanics Mining Science & Geomechanics Abstracts 1996;33(8):785–802.
[3] Lomize GM. Water flow through jointed rock. Moscow: Gosenergoizdat, 1951 (in Russian).
[4] Snow DT. A parallel plate model of fractured permeable media. PhD Thesis, Univ of California. 1965. 331 pp.
[5] Iwai K. Fundamental studies of fluid flow in a single fracture. PhD Thesis, Univ. of California. 1976. 208 pp.
[6] Gangi AF. Variation of whole- and fractured-porous-rock permeability with confining pressure. Int J Rock Mech Min Sci & Geomech Abstr 1978;15:249–57.
[7] Witherspoon PA, Wang JS, Iwai K, Gale JE. Validity of cubic law for fluid flow in a deformable rock fracture. Water Resources Res 1980;16(6):1016–24.
[8] Engelder T, Scholz CH. Fluid flow along very smooth joints at effective pressure up to 200 megapascals. Mechanical Behavior of Crustal Rocks. Amer Geophys Union Monograph 1981;24:147.
[9] Raven KG, Gale JE. Water flow in a natural rock fracture as a function of stress and sample size. Int J Rock Mech Min Sci & Geomech Abstr 1985;22(4):251–61.
[10] Pyrak-Nolte LJ, Myer LR, Cook NGW, Witherspoon PA. Hydraulic and mechanical properties of natural fractures in low permeability rock. In: Herget G, Vongpaisal S, editors. Proceedings of the Sixth International Congress on Rock Mechanics, Montreal, Canada. August 1987. Rotterdam: Balkema, 1987. p. 225–31.
[11] Gale JE. Comparison of coupled fracture deformation and fluid models with direct measurements of fracture pore structure and stress-flow properties. In: Farmer IW, Daemen JJK, Desai CS, Glass CE, Neuman SP, editors. Rock Mechanics: Proceedings of the 28th US Symposium. Tucson, Arizona. Rotterdam. Rotterdam: Balkema, 1987. p. 1213–22.
[12] Tsang YW, Tsang CF. Channel model of flow through fractured media. Water Resources Res 1987;23:467.
[13] Pyrak-Nolte LJ, Cook NGW, Nolte DD. Fluid percolation through single fractures. Geophysical Research Letters 1988;15(11):1247–50.
[14] Hakami E. Water flow in single rock joints. Licentiate. Thesis. Lulea University of Technology, Sweden, 1988.
[15] Zimmerman RW, Kumar S, Bodvarsson GS. Lubrication theory analysis of the permeability of rough-walled fractures. Int J Rock Mech Min Sci & Geomech Abstr 1991;28(4):325–31.
[16] Iwano M, Einstein HH. Laboratory experiments on geometric and hydromechanical characteristics of three different fractures in granodiorite. In: Fujui T, editors. Proceedings of the Eight International Congress on Rock Mechanics, vol. 2. Rotterdam: Balkema, 1995. p. 743–50.
[17] Durham WB, Bonner BP. Closure and fluid flow in discrete fractures. In: Myer LR, Cook NGW, Goodman RE, Tsang CF, editors. Fractured and Jointed Rock Masses. Rotterdam: Balkema, 1995. p. 441–6.
[18] Kranz RL, Frankel AD, Engelder T, Scholz CH. The permeability of whole and jointed barre granite. Int J Rock Mech Min Sci & Geomech Abstr 1979;16:225–34.
[19] Brown SR. Fluid flow through rock joints: The effect of surface roughness. J Geophys Res 1987;92:1337–47.
[20] Tsang YW. The effect of tortuosity on fluid flow through a single fracture. Water Resources Res 1984;20(9):1209–15.
[21] Pyrak-Nolte LJ, Montemagno CD, Nolte DD. Volumetric imaging of aperture distributions in connected fracture networks. Geophys Res Let 1997;24(18):2343–6.
[22] Keller AA. High resolution cat imaging of fractures in consolidated materials. In: Kim K, editors. Proceedings for the 36th U.S. Rock Mechanics Symposium and ISRM International Symposium, vol. 1. New York: Columbia University, 1997. p. 97–106.
[23] Durham WB. Laboratory observations of the hydraulic behavior of a permeable fracture from 3800 m depth in the KTB pilot hole. J Geophys Res 1997;102(B9):18405–16.
[24] Gentier S, Billaux D, van Vliet L. Laboratory testing of the voids in a fracture. Rock Mechanics and Rock Engineering 1989;22:149–57.
[25] Hakami E. Joint aperture measurements — An experimental technique. In: Myer LR, Cook NGW, Goodman RE, Tsang CF, editors. Fractured and Jointed Rock Masses. Rotterdam: Balkema, 1995. p. 453–6.
[26] Hakami E, Barton N. Aperture measurements and flow experiments using transparent replicas of rock joints. In: Barton, Stephannson, editors. Rock Joints. Rotterdam: Balkema, 1990. p. 383–90.
[27] Gentier S. Morphological analysis of a natural fracture. Selected papers from the 28th Int. Geological Congress. Washington, DC, 9–19 July, 1989 [special issue]. Hydrogeology 1990;1:315–26.
[28] Montemagno CD, Pyrak-Nolte LJ. Fracture network versus single fractures: Measurement of fracture geometry with X-ray tomography. J Phyisics and Chemistry of the Earth 1999;24(7).
[29] Duncan N, Hancock KE. The concept of contact stress in assessment of the behavior of rock masses as structural foundations. In: Proc. First Congress Int. Soc., Rock Mech., vol. 2. Lisbon, 1966. p. 487–92.
[30] Bandis SC, Luden AC, Barton NR. Fundamentals of rock joint deformation. Int J Rock Mech Min Sci & Geomech Abstr 1983;20(6):249–68.
[31] Nolte DD, Pyrak-Nolte LJ. Stratified continuum percolation — scaling geometry of hierarchical cascades. Phys Rev A 1991;44(10):6320–33.
[32] Zimmerman RW, Chen DW, Long JCS, Cook NGW. Hydromechanical coupling between stress, stiffness, and hydraulic conductivity of rock joints and fractures. In: Barton, Stephansson, editors. Rock Joints. Rotterdam: Balkema, 1990. p. 571–7.
[33] Goodman RE. In: Methods of geological engineering in discontinuous rock. New York: West, 1976. p. 172.
[34] Swan G. Determination of stiffness and other joint properties from roughness measurements. Rock Mech Rock Engng 1983;16:19–38.
[35] Barton NR, Bandis S, Bakhtar K. Strength, deformation and conductivity coupling of rock joints. Int J Rock Mech Min Sci & Geomech Abstr 1985;22(3):121–40.
[36] Brown SR, Scholz CH. Closure of random surfaces in contact. J Geophys Res 1985;90(B7):5531–45.
[37] Brown SR, Scholz CH. Closure of rock joints. J Geophys Res 1986;91:4939.
[38] Hopkins DL, Cook NGW, Myer LR. Fracture stiffness and aperture as a function of applied stress and contact geometry. In: Farmer IW, Daemen JJK, Desai CS, Glass CE, Neuman SP, editors. Rock Mechanics: Proceedings of the 28th US Symposium. Tucson, Arizona. Rotterdam: Balkema, 1987. p. 673–80.
[39] Hopkins DL, Cook NGW, Myer LR. Normal joint stiffness as a function of spatial geometry and surface roughness. In: Barton, Stephansson, editors. Rock Joints. Rotterdam: Balkema, 1990. p. 203–10.
[40] Kendall K, Tabor D. An ultrasonic study of the area of contact between stationary and sliding surfaces. Proc Royal Soc London, Series A 1971;323:321–40.
[41] Pyrak-Nolte LJ. Interrelationship between the hydraulic and seismic properties of fractures. In: Myer LR, Cook NGW, Goodman RE, Tsang CF, editors. Fractured and Jointed Rock Masses. Rotterdam: Balkema, 1995. p. 111–7.

[42] Pyrak-Nolte LJ, Myer LR, Cook NGW. Transmission of seismic waves across natural fractures. Journal of Geophysical Research 1990;95(B6):8617–38.
[43] Pyrak-Nolte LJ, Xu J, Haley GM. Elastic interface waves propagating in a fracture. Physical Review Letters 1992;68(24):3650–3.
[44] Gale JE. The effects of fracture type (induced versus natural) on stress–fracture closure–fracture permeability relationships. In: Issues in Rock Mechanics: Proceedings of the 23rd US Symposium on Rock Mechanics. Rotterdam: Balkema, 1982. p. 290–8.
[45] Hopkins DL. The Effect of Surface Roughness on Joint Stiffness, Aperture, and Acoustic Wave Propagation. PhD Thesis, University of California at Berkeley, 1990.
[46] Timoshenko SP, Goodier JN. Theory of elasticity. 3rd ed. New York: McGraw-Hill, 1970.
[47] Golub GH, Van Loan CF. Matrix Computations. 2nd ed. Baltimore: Johns Hopkins University Press, 1989 Chapters 4 and 10.
[48] Guyer RA, Johnson PA. Nonlinear mesoscopic elasticity. Physics Today 1999;52(4):30–6.
[49] Greengard L, Rokhlin. The Rapid Evaluation of Potential Fields in Particle Systems. Cambridge, Mass: MIT Press, 1988.
[50] Unger AJA, Mase CW. Numerical study of the hydromechanical behavior of two rough fracture surfaces in contact. Water Resources Research 1993;29(7):2101–14.
[51] Yang G, Cook NGW, Myer LR. Network modelling of flow in natural fractures. In: Rock Mechanics as a Guide for Efficient Utilization of Natural Resources, 1989. p. 57–64.
[52] Tran JJ. Efficient simulations of multiphase flow in three-dimensional fracture networks. PhD Thesis, Department of Computer Science and Engineering, University of Notre Dame, IN, 1998.
[53] Morris JP, Jiangtao Cheng, Tran JJ, Lumsdaine A, Giordano NJ, Pyrak-Nolte LJ. Single phase flow in a fracture: Micromodel experiments and ab-initio simulation, 1999 (in preparation).
[54] Blair SC, Berge PA, Berryman JG. Two-point correlation functions to characterize microgeometry and estimate permeabilities of synthetic and natural sandstones, Lawrence Livermore National Laboratory report, UCRL-LR-114182, 1993.
[55] Berryman JG. Relationship between specific surface area and spatial correlation functions for anisotropic porous media. J Math Phys 1987;28(1):244–5.
[56] Brown SR, Kranz RL, Bonner BP. Correlation between the surfaces of natural rock joints. Geophysical Research Letters 1986;13:1430–4.
[57] Pyrak-Nolte LJ. Thesis, 1988.
[58] Pyrak-Nolte LJ, Cook NGW, Myer LR. Effect of stress on hydraulic, mechanical and seismic properties of a natural fracture. Transactions American Geophysical Union 1986;67(16):272.
[59] Nolte DD, Pyrak-Nolte LJ, Cook NGW. Fractal geometry of the flow paths in natural fractures and the approach to percolation. Pure and Applied Geophysics 1989;131(1/2):111.
[60] Pyrak-Nolte LJ, Myer LR, Nolte DD. Fractures: Multifractals & finite-size scaling. Pure and Applied Geophysics 1992;138(4):679–706.